PNAS RESEARCH ARTICLE | ENGINEERING

Tautomerism induces bending and twisting of biogenic crystals

Weiwei Tang[a,b], Taimin Yang[c], Qing Tu[d], Hector A. Calderon[e,f], Francisco C. Robles Hernandez[g], Padraic O'Reilly[h], Yun Jing[h], Sung Park[h], and Jeffrey D. Rimer[a,1]

Affiliations are included on p. 8.

Edited by Joanna Aizenberg, Harvard University, Allston, MA; received December 21, 2024; accepted June 13, 2025

Understanding and exploiting material flexibility through phenomena such as the bending and twisting of molecular crystals has been a subject of increased interest owing to the number of applications that benefit from these properties, such as optoelectronics, mechanophotonics, soft robotics, and smart sensors. Here, we report the growth of spontaneously bent and twisted ammonium urate crystals induced by the keto–enol tautomerism of the urate molecule. The major tautomer is native to biogenic crystals, whereas the minor tautomer functions as an effective crystal growth modifier to induce naturally bent and twisted ammonium urate crystals. We show that the degree of curvature can be tailored based on the judicious selection of growth conditions. A combination of state-of-the-art microscopy and spectroscopy techniques are used to characterize the origin of bending. Spatially resolved nano-electron diffraction and high-resolution electron microscopy of naturally bent crystals show nearly single crystallinity with local lattice deformations generated by a combination of screw and edge dislocations. These observations are consistent with photoinduced force microscopy and contact resonance atomic force microscopy, which confirmed spatially resolved changes in the intermolecular interactions and the mechanical properties throughout the cross-sectional and axial regions of bent crystals. A mechanism of bending involving the generation of regionally specific dislocations is proposed as an alternative to more commonly reported models. These findings highlight a unique characteristic of tautomeric crystals that may have broader implications for other biogenic materials.

tautomer | crystallization | bending | biogenic | crystal engineering

Significance

The bending and twisting of crystalline materials are essential characteristics for many applications where flexibility is critical; however, well-defined structure–property relationships and molecular design strategies for achieving bent and/or twisted crystals in situ remain elusive. Here, we present a unique case of natural bending without the application of external forces. This is a mechanistic investigation showing how tautomerism induces controlled, natural bending and twisting by virtue of the minor tautomer, which is a growth modifier that causes defects in the crystal structure (e.g., twins, screw and edge dislocations), leading to macroscopic effects on material properties. This work offers potential routes for crystal engineering that can be leveraged for diverse materials to selectively tailor their properties.

Recently, there has been increased interest in flexible organic bending and twisted crystals due to their unique properties for flexible optoelectronics (1–4), mechanophotonics (5–7), soft robotics (8–10), and smart sensors (11). Bent and twisted crystal growth has been observed for a variety of natural and synthetic inorganic materials (12, 13), such as quartz (14), dolomite (15), and jamesonite (16). In these systems, crystal bending or twisting is attributed to spontaneous mechanical transformation over the course of growth. These transformations are typically triggered by intrinsic factors such as twinning, point and linear defects such as edge and screw dislocations, surface stress, inhomogeneous thermal, mechanical, or compositional fields, as well as heterometry stress (12). However, in the regime of organic molecular crystals, it is less common to observe natural bending or twisting, particular for crystals derived from supersaturated solutions. Spherulites of organic molecules with twisted mesoscale fibers can grow from slightly undercooled melts (12, 17). Only in few cases, bent or twisted crystals from solutions have been reported (18–20). This phenomenon is usually caused by phase impurities (19, 21), photoinduced processes (22), or harsh synthetic conditions (e.g., high rate of solvent evaporation) (18). However, simultaneous observation of bending and twisting in organic crystals is relatively scarce and generally attributed to cocrystals. One recent example indicates that the twisted (E)-2-[((5-ethoxypyridin-2-yl)imino)-methyl]phenol and 1,3,5-trifluoro-2,4,6-triiodobenze ne cocrystals can also display natural bending (23). Crystal deformation is nonintrinsic to the majority of organic crystals but can be induced via external stimuli, such as light (10, 24–26), heat (27), or mechanical forces (28–33). In general, molecular design strategies for achieving these morphologies are elusive; and many of the external methods used to induce plastic deformation, such as tweezers, mechanical probes, or microcantilevers (10, 30, 34, 35), are time-consuming processes. This motivates the development of facile methods to produce organic molecular crystals with controllable curvature in situ.

In a previous study (36) we reported that tautomerism can induce defects during crystallization that generate unique morphologies. Tautomers are structural isomers that are ubiquitous in synthetic (37–39) and biological crystals as either small organic molecules (40) or macromolecules (e.g., peptides, nucleic acids, and proteins) (41). They play a central role in the development of crystalline materials with diverse optical (42), magnetic

Author contributions: W.T. and J.D.R. designed research; W.T. performed research; H.A.C. contributed new reagents/analytic tools; W.T., T.Y., Q.T., H.A.C., F.C.R.H., P.O., Y.J., S.P., and J.D.R. analyzed data; and W.T. and J.D.R. wrote the paper.

The authors declare no competing interest.

This article is a PNAS Direct Submission.

[1]To whom correspondence may be addressed. Email: jrimer@central.uh.edu.

This article contains supporting information online at https://www.pnas.org/lookup/suppl/doi:10.1073/pnas.2426814122/-/DCSupplemental.

Published July 21, 2025.

(43), electrical (44), and chemical (45) properties. For example, biogenic organic flexible crystals derived from tautomers are compliant with the body's immune system and can be molded and shaped into new biocompatible plastic materials as actuators and sensors with a variety of potential biomedical applications (46). This class of structural isomers can undergo interconversions via intramolecular relocation of atoms, most commonly hydrogens in processes referred to as prototropic tautomerism (47). Despite numerous studies reporting crystals of tautomeric species, their roles in crystal growth and ability to induce crystal bending or twisting are underexplored.

Here, we show that native tautomerism of urate molecules in aqueous solutions induces bending and twisting of ammonium urate (NH_4HU) crystals, which may provide a bottom–up approach to achieve these properties without any required external stimuli other than the adjustment of solution pH. Urate is a prototypical tautomeric compound and is generated from the endogenous metabolism of two purine nucleic acids, i.e., adenine and guanine, in the liver, intestines, and kidneys (48–51). In a previous study, we discovered that the diketo–enol $[DKE\text{-}N_9]^-$ species, which is the minor tautomer (non-native to the crystal structure), functions as an inhibitor to suppress the growth of NH_4HU crystals (36). The effects of the minor tautomer at low and high supersaturation can lead to crystal bending and branching, respectively. Herein, we report that defects imposed by a minor tautomer can result in simultaneous bending and twisting *via* synergistic processes that lead to morphologies consistent with those of biogenic NH_4HU crystals. We use multiple state-of-the-art techniques to resolve the origin of defects and propose a mechanism for spontaneous (bottom–up) bending and twisting of organic crystals that may prove to be more broadly applicable to other tautomeric materials.

Results and Discussion

In aqueous solution, urate exists in its neutral form in acidic media and exhibits a negative charge in neutral and basic media (−1 or −2, respectively). Negatively charged urates are tautomers (Fig. 1*A*), or structural isomers, where diketo–enol $[DKE\text{-}N_3]^-$ is native to the crystal structure of ammonium urate and its minor tautomer, diketo–enol $[DKE\text{-}N_9]^-$, is present in appreciable quantity (11%). We previously reported that the minor tautomer functions as an inhibitor of NH_4HU crystal growth (36). In alkaline solutions (pH 11) NH_4HU crystallizes as straight rods (36); however, at neutral conditions (pH 7) it is common to observe natural bending of crystals (Fig. 1*B*). The crystallinity of bent crystals was confirmed by powder X-ray diffraction (*SI Appendix*, Fig. S1). These effects are most evident when urate concentrations are below 7 mM. In general, the degree of NH_4HU crystal bending is correlated to urate concentration. For example, in mildly supersaturated solutions (5 mM) the resulting crystals are slightly bent (Fig. 1*C*); however, at higher urate concentration (7 mM) the bending is significantly more pronounced, resulting in complete "loops" (Fig. 1*D*) that are characteristic of many soft materials (e.g., polymers). Scanning electron microscopy (SEM) images reveal that all crystals are bent, but high-magnification SEM

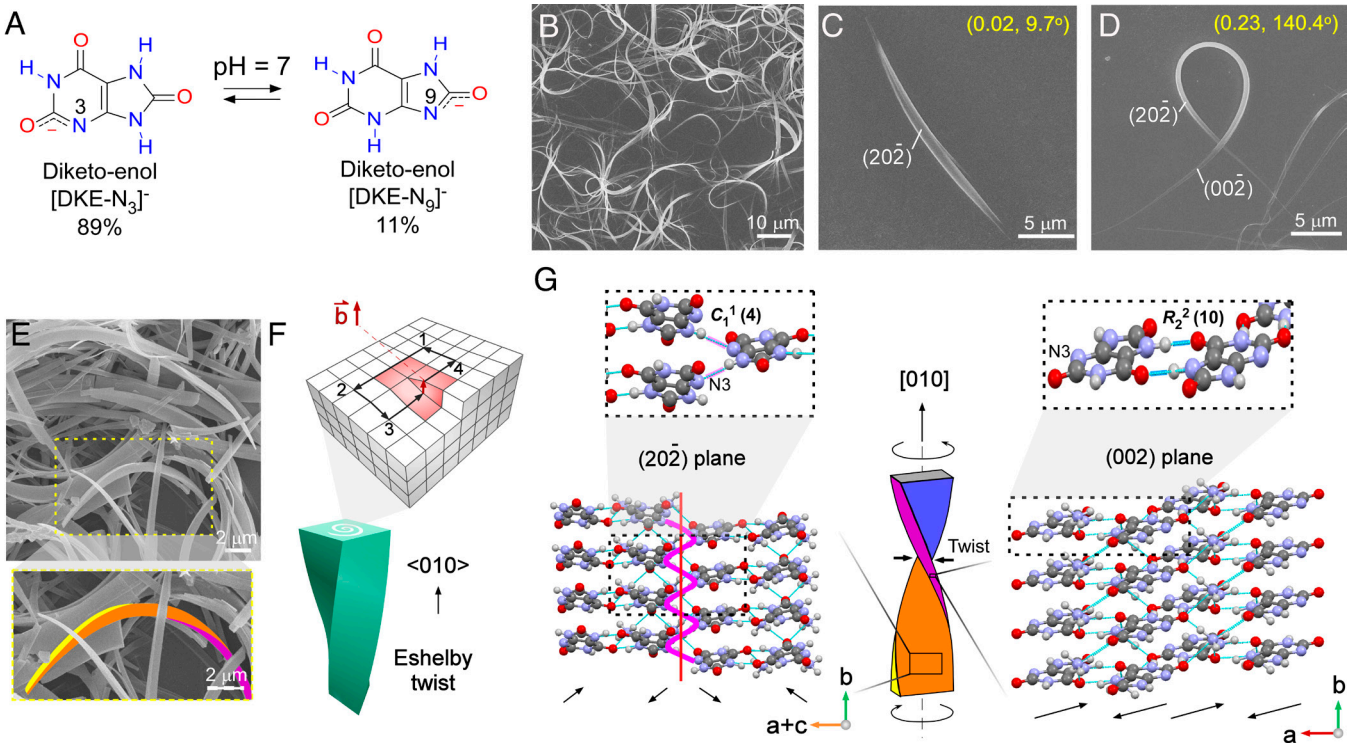

Fig. 1. (*A*) Molecular structures of urate, HU^-, tautomers: $[DKE\text{-}N_3]^-$ (major) and $[DKE\text{-}N_9]^-$ (minor). (*B–D*) Scanning electron micrographs of NH_4HU crystals prepared at pH 7 with urate concentrations, C_{urate}, of (*B*) 7 mM, (*C*) 5 mM, and (*D*) 7 mM. The values in yellow font, (κ_{avg}, α_{max}), represent the average curvature, κ_{avg}, and the maximum bending angle, α_{max}, of a bent NH_4HU crystal. (*E*) Higher magnification SEM image of crystals prepared at C_{urate} = 6 mM. Callout: expanded image of the yellow dashed box showing different facets (colored segments) of a crystal exhibiting both bending and twisting. Note that we only include a left-handed crystal for illustrative purposes, whereas statistical analysis of SEM images reveals equal number of left- and right-handed crystals (*SI Appendix*, Fig. S2). (*F*) Schematic representation of Eshelby twist originating from an axial screw dislocation along the <010> direction with Burgers vector (red arrow). (*G*) Facets of a twisted NH_4HU crystal indexed by TEM tomography. The hydrogen-bonded 2_1 helix is indicated by the curved magenta line in the (20$\bar{2}$) plane, and dashed cyan lines are hydrogen bonds in both the (20$\bar{2}$) and (002) planes. Callout: (*Left*) expanded image of the black dashed box highlighting π–π stacking columns (intermolecular distance of 3.342 Å) linked by $C_1^1(4)$ hydrogen bonding chain; (*Right*) expanded image of the black dashed box highlighting urate–urate hydrogen bonding dimers, $R_2^2(10)$. Note for clarity the ammonium ions were deleted in the expanded image, and N3 atom in urate is only involved in the formation of hydrogen bonding chain, not dimers. Black arrows indicate different urate orientations within the crystal structure.

images also reveal that a majority of crystals are also twisted (Fig. 1*E*). The degree of twisting varies among crystals prepared in a given batch, and the relative percentage of crystals that are both bent and twisted appears to increase with urate concentration. The region of NH_4HU crystals where twisting is most readily observed is near the ends of needles (e.g., callout in Fig. 1*E* and *SI Appendix*, Fig. S2), reminiscent of the Eshelby twist mechanism in inorganic crystalline materials (52, 53). Eshelby has shown that an axial screw dislocation at the center of a thin rod-like crystal will create a stress field that exerts torque at the free ends of the cylinder (Fig. 1*F*), resulting in crystal twisting along the axial direction (54), analogous to our observation of NH_4HU crystals. The left-handed and right-handed crystals are nearly equal in number (*SI Appendix*, Fig. S2). Interestingly, we found that the majority of twisted crystals display a "C-shaped" bending morphology (*SI Appendix*, Fig. S2) where half of the bent crystal exhibits right-handedness and the other half has a left-handedness; however, the sides of bent crystals are not fully symmetric. A rough estimation suggests that the pitch may be in the range of millimeters, which is similar to other inorganic crystalline materials (e.g., ZnS whiskers) (55) and aligns with the large pitch predicted by the Eshelby twist mechanism (12, 56).

The facets of bent and twisted NH_4HU crystals were indexed using transmission electron microscopy (TEM) tomography (*SI Appendix*, Fig. S3 and Movies S1 and S2). Bending occurs along the b-axis, normal to the [010] axial direction of needles, while the crystal twists by winding of the $(20\bar{2})$ and (002) planes along the [010] direction. The crystal structure of NH_4HU (*C2/c* space group, *SI Appendix*, Fig. S4) consists of four distinct orientations of urate molecules as indicated by the arrows in Fig. 1*G* (36). The $(20\bar{2})$ plane comprises π–π stacking columns (Fig. 1*G*) of urate–urate hydrogen-bonding dimers that are linked through a hydrogen-bonding 2_1 helix (Fig. 1*G*, magenta line). The (002) plane comprises urate dimers that are interconnected by N–H···O hydrogen bonds (Fig. 1*G*, dashed cyan lines) forming hydrogen-bonding sheets comprising N–H···N and electrostatic ammonium–urate interactions (*SI Appendix*, Figs. S4–S6). These relatively weak interactions in the c-plane generate an interface between the layers that can facilitate gliding of edge dislocations during bending, whereas disruption of the 2_1 helical molecular assembly along the [010] direction may facilitate crystal twisting (*vide infra*). According to the theory of Eshelby (12), the twist rate is $\alpha = \pi/P = \kappa b/A$ where *P* is the pitch of twist, *b* is the magnitude of the Burgers vector of the screw dislocation, κ is a prefactor related to crystal geometry, and *A* is the crystal cross-sectional area. The Burgers vector for an axial screw dislocation should be parallel to the longitudinal <010> growth direction, and its magnitude is a fraction of the lattice parameter (ca. 0.17 nm). A typical NH_4HU rod-like crystal is less than 1 μm in width and 0.2 to 0.5 μm in thickness, resulting in A = 0.2 to 0.5 μm^2. On this basis, we estimate the pitch should be around 3 to 9 mm, which is in reasonable agreement with SEM images (*SI Appendix*, Fig. S2).

In order to quantify the degree of bending, we performed a statistical analysis of optical micrographs of more than 80 crystals prepared in neutral growth solutions (pH 7) at three different urate concentrations (5, 6, and 7 mM). As shown in the inset of Fig. 2*A*, the geometry of a bent crystal can be described by three parameters (*SI Appendix*, Fig. S7): the bending angle, α; the radius of curvature, ρ; and the curvature, $\kappa = 1/\rho$. We examined NH_4HU crystals prepared at the lowest urate concentration (Fig. 2*A*) and observed a relatively narrow distribution of curvature with an average value of 0.02 μm^{-1}. At the intermediate urate concentration, the distribution slightly widens and the average κ increases to 0.05 μm^{-1}; and at the highest urate concentration, the distribution is broader (i.e., approximately Gaussian) with an average κ of 0.12 μm^{-1}. The dislocation density may be estimated from the bending curvature assuming continuously varying distributions of dislocations and no elastic stretching of the Burgers circuit (57). The average density of edge dislocations is about 2×10^{13} m^{-2} at the lowest urate concentration and increases up to 1.2×10^{14} m^{-2} at the highest urate concentration. These values are in reasonable agreement with those derived from powder X-ray diffraction data, which account for both edge and screw dislocations (*SI Appendix*, Table S1). We find that the dislocation density in bent/twisted NH_4HU crystals is significantly greater than those predicted in literature for high-quality crystals (10^5–10^8 m^{-2}) but slightly lower than those of crystals grown from melt (10^{14}–10^{16} m^{-2}) (58). The increasing curvature and dislocation density with higher supersaturation is consistent with visual observation of more acutely bent crystals in both optical and scanning electron micrographs (*SI Appendix*, Figs. S8 and S9). Analysis of corresponding bending angles at all three concentrations (Fig. 2*D* and *SI Appendix*, Fig. S8 *D–F*) also reveals that increased bending with higher urate supersaturation leads to NH_4HU crystals with reduced thickness.

Our previous study (36) showed a unique trend of NH_4HU crystal growth rate as a function of urate supersaturation wherein a region of bending at lower concentrations shifts to a relatively narrow region of growth cessation, followed by rapid increase in growth rates at higher supersaturations where branching leads to dumbbell-shaped crystals that can transition into spherulites (36, 48). All measurements in the prior study were performed with growth solutions containing NaCl where in situ atomic force microscopy (AFM) and microfluidics both confirmed the distinct growth regimes. In this current study, we use growth solutions without NaCl to minimize the degree of branching. In situ AFM measurements of surface growth using NaCl-free media reveal nearly identical trends in growth rate (i.e., step velocity) with increasing urate supersaturation (*SI Appendix*, Fig. S11). AFM analysis of the rate of two-dimensional island nucleation, J_{2D}, on basal $(20\bar{2})$ surfaces shows very little change with urate concentration in the regime prior to growth cessation where bending is most evident (Fig. 2*E*, gray shading). Under these conditions surface growth still proceeds by a classical layer-by-layer mechanism, but the rate of 2D island generation is relatively low; however, at higher urate concentrations in the regime where branching is more prevalent (Fig. 2*E*, green shading) there is a significant change in J_{2D} with a monotonically increasing trend with supersaturation. The same conditions were tested in microfluidics using NH_4HU seeds prepared in alkaline solution (pH 11) to achieve initially straight crystals for more facile observation of bending during in situ seeded growth at pH 7. Interestingly, we do not observe significant bending during seeded growth at low urate concentration (Fig. 2*F*, 6 mM), but we do observe tapering at the ends of rod-like crystals (Fig. 2 *I* and *J*), consistent with prior findings where we related this phenomenon to the effect of minor tautomer adsorption near crystal edges (36).

Under conditions where we observe crystal bending and twisting (5 to 8 mM urate), we infer the presence of screw dislocations from the kinetics of NH_4HU crystal growth along the <010> direction (Fig. 2*K*). The rate of growth along the <010> direction, $r_{<010>}$, displays a nearly linear trend ($R^2 = 0.993$) with supersaturation, σ (*SI Appendix*, Fig. S12), which is in agreement with the Burton-Cabrera-Frank (BCF) model of classical surface growth (59). A linearized plot of $\ln r_{<010>}$ *versus* $\ln \sigma$ (Fig. 2*K*) gives a slope of 1.2, which is within the range of the BCF model for screw dislocations that are often generated under mild growth conditions (i.e., low urate concentrations) (60). Indeed, we observe twisted

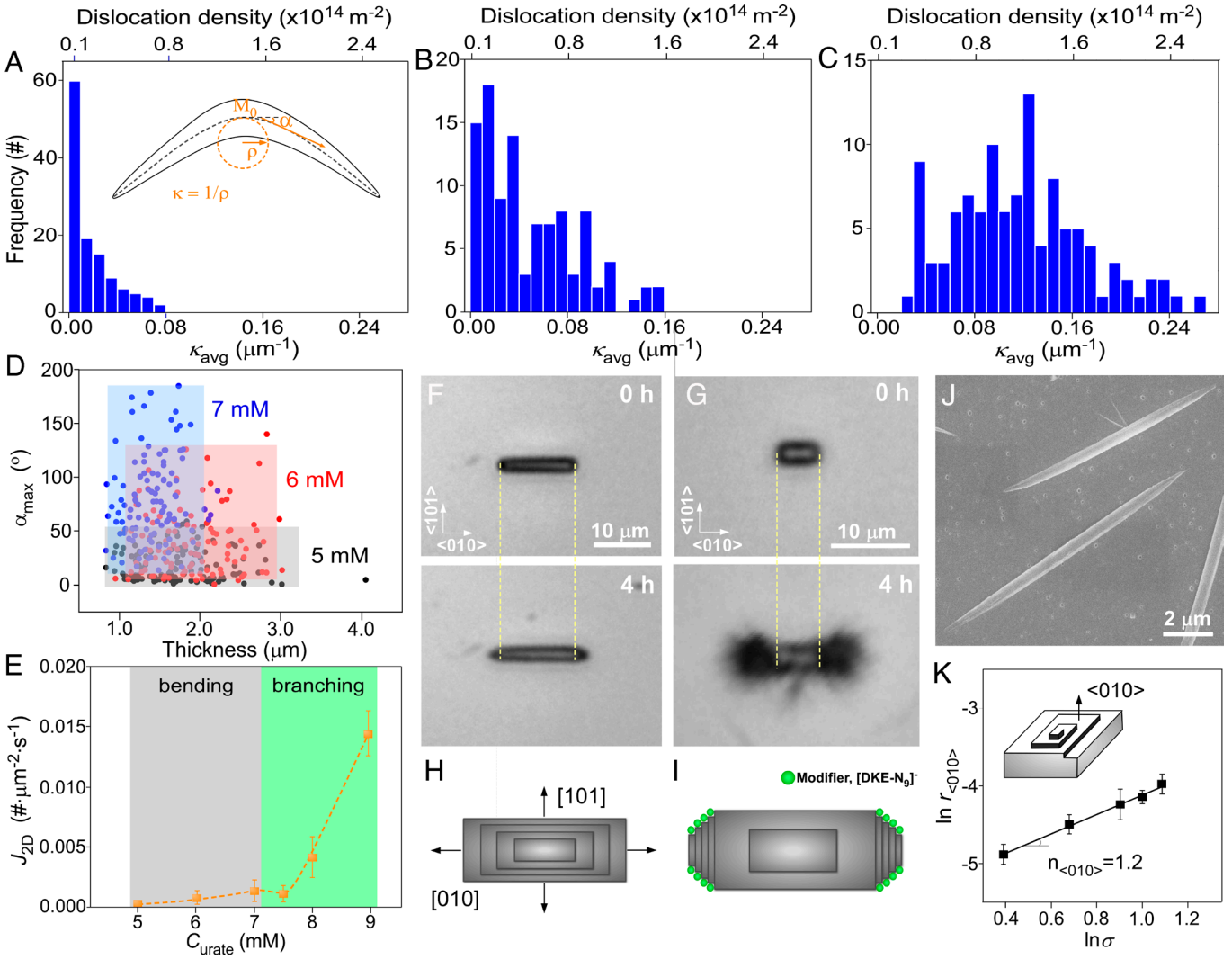

Fig. 2. (*A–C*) Statistical analysis of the average curvature κ_{avg} (*Bottom* x-axis) and estimated dislocation density (*Top* x-axis) for NH_4HU crystals prepared at three different urate concentrations: (*A*) 5 mM, (*B*) 6 mM, and (*C*) 7 mM. (*A*, *Inset*) Illustration of a bent crystal highlighting various geometrical parameters: α represents the bending angle at a particular point on a bent crystal and ρ is the radius of curvature ($\rho = 1/\kappa$). (*D*) The maximum bending angle, α_{max}, as a function of NH_4HU crystal thickness for samples prepared at 5 mM (gray), 6 mM (red), and 7 mM (blue) urate concentrations. (*E*) Atomic force microscopy measurements of the rate of 2D island nucleation, J_{2D}, on the $(20\bar{2})$ surface of NH_4HU crystals as a function of C_{urate}. Shaded regions correspond to the visual observation of crystal bending (gray) and branching (green) during bulk crystallization. Symbols are the average of 25 to 40 measurements and error bars span two SD. (*F* and *G*) In situ microfluidic measurements of seeded growth in (*F*) 6 mM and (*G*) 10 mM urate solutions at pH 7. (*H* and *I*) Schematic representation of NH_4HU crystal habit in the absence of modifier (i.e., minor tautomer) (*H*) and with tapering due to enhanced adsorption of the minor tautomer (green spheres) near crystal edges (*I*). (*J*) SEM image of representative NH_4HU crystals after microfluidic growth in 6 mM urate solutions showing tapering. (*K*) Linearized plot of growth rates, $\ln r_{<010>}$ versus $\ln \sigma$, revealing a nearly linear dependence on supersaturation ($r \propto \sigma^{1.2}$) with a slope of n = 1.2, which is suggestive of a spiral growth mechanism (59).

NH_4HU crystals only form at relatively low urate concentrations, whereas higher supersaturation leads to crystal branching (*SI Appendix*, Fig. S9*D*). AFM studies also confirm a shift in the surface growth mechanism from low to high urate concentrations (Fig. 2*E*). Likewise, time-resolved images of seeded crystal growth in the microfluidic channel reveal a high degree of branching (Fig. 2*G*) in concentrated solutions (10 mM urate), in agreement with SEM images (*SI Appendix*, Fig. S13).

Nano-electron diffraction (NED) analysis of a bent NH_4HU crystal (Fig. 3*A*) was used to investigate potential changes in lattice parameters along the cross-section direction at three distinct locations: regions 1 (orange), 2 (green), and 3 (blue) spanning from convex (cx) to concave (cc) sides. Representative NED patterns (Fig. 3*A*, *Insets*) confirm a high degree of single crystallinity in local regions of the bent crystal compared to evidence of defects when the area of diffraction is larger (*SI Appendix*, Fig. S14). From these data, we measured the interplanar $d_{(hkl)}$ spacing of (002), (200), and (202) planes at each location and compare the results to the reported NH_4HU crystal structure obtained from a straight (str), relatively defect-free crystal (36). There is no apparent change in the (200) d-spacing along the cross-section direction (Fig. 3*B* and *SI Appendix*, Fig. S15); however, there is a larger (202) d-spacing at all locations of the bent crystal, which is consistent with twisting along the 2_1 helix in the [010] direction (Fig. 1*G*). The most dramatic change is the (002) d-spacing, observed only on the convex side, which increases from 0.917 to 0.985 nm compared to the straight crystal. The significant shift in the (002) lattice is consistent with a gliding of planes between hydrogen-bonding sheets depicted in Fig. 1*G* that occurs during bending.

High-resolution transmission electron microscopy (HRTEM) images of bent NH_4HU crystals have been collected under low dose conditions with stacking of at least 20 experimental images (dose fractionalization) in order to preserve the genuine structure of the sample at the ultimate detection limit. The intention is to use small doses along with relaxations to make sure that the

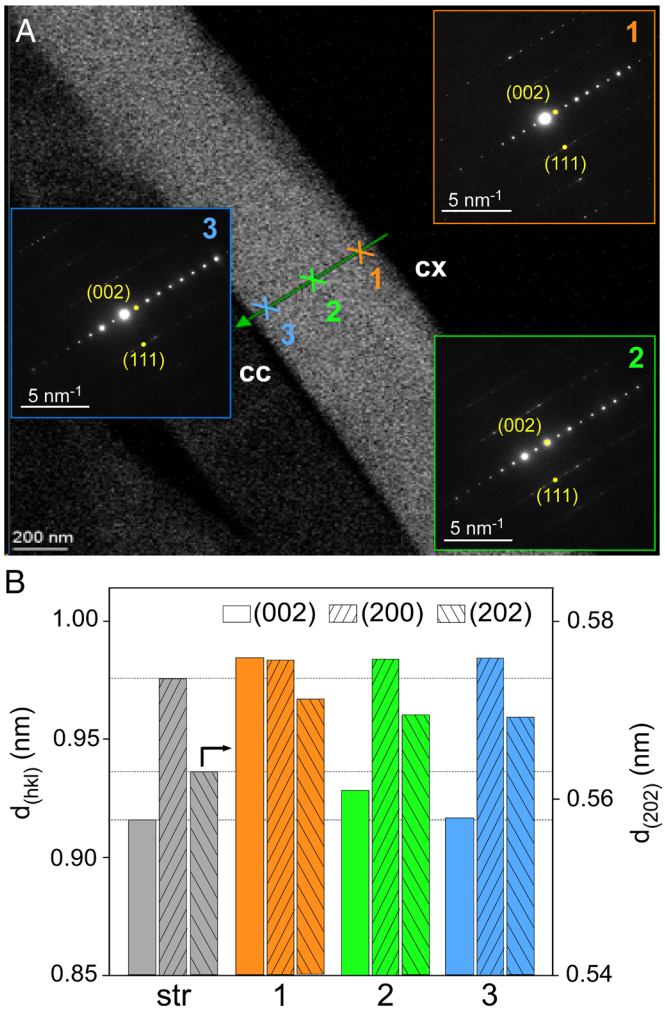

Fig. 3. Spatially resolved nano-electron diffraction (NED) analysis of a bent NH_4HU crystal. (*A*) Representative TEM image highlighting three local regions measured in the direction of the green arrow: convex side (1, orange), near the middle (2, green), and concave side (3, blue). Insets: corresponding NED patterns in the [1$\bar{1}$0] zone axis at each region along the cross-section direction of a bent NH_4HU crystal segment. (*B*) Interplanar $d_{(hkl)}$ spacing of (002), (200), and (202) planes at the regions along the cross-section direction compared to the reported values for a straight, nearly defect-free single crystal (str).

structure is preserved and genuine. The beam sensitivity of the sample restricts the number of images that can be acquired; however, the observation technique allows monitoring the potential structure degradation with dose accumulation. This low-dose fractionation technique enables the imaging of different structural defects of a bent organic crystal with atomic resolution. HRTEM images of a straight segment in a bent crystal (Fig. 4 *A* and *B*) show with remarkable resolution highly crystalline domains with almost perfect arrays of atomic clusters of molecules. The simulated projection along the image zone axis [00$\bar{1}$] (Fig. 4 *A*, *i*, green box) is an excellent match to the overlayed crystal structure (Fig. 4*B*). The straight segments contain random distortions (Fig. 4 *A, ii*, blue box) where magnified images (Fig. 4*C*) show stacking faults that are associated with dislocations (61, 62). We posit these defects are generated as a result of perturbations in aromatic stacking.

HRTEM images of bent segments detect much higher percentages of defects that likely cause the natural deformation of NH_4HU crystals. Fig. 4*D* shows a bent segment where analysis has been performed both axially and along the cross-section. The concave side of the cross-section [image (iii) in Fig. 4*D*] has no apparent defects; however, the convex side [image (iv) in Fig. 4*D*] contains 2D and 1D defects such as twins, edge and screw dislocations, which is consistent with the observed shifts in (002) and (202) d-spacings in Fig. 3. This may explain why electron micrographs of bent NH_4HU crystals tend to show branching (*SI Appendix*, Fig. S16) that seems to originate on the convex-side of rod-like crystals that gives rise to sheath-like morphologies. A higher defect density in this region is also reflected in fast Fourier transformation (FFT) patterns, which show an increased d-spacing (*SI Appendix*, Fig. S17*A*) from concave to convex sides that agree with NED analysis (Fig. 3). For straight segments containing few defects, the (31$\bar{1}$) d-spacing is 0.31 nm. Analysis along the axial b-direction of a bent segment (from region 1 to 7 in Fig. 4*D*) shows that the (31$\bar{1}$) d-spacing monotonically decreases from 0.33 to 0.29 nm (Fig. 4*E*). This result is a reflection of a gradually enlarged separation of the lattice along the axial (fast) growth direction; and with this change we observe a concomitant shift in the b-direction orientation, which is quantified by the angle $\emptyset$ = [010]$\cap$ [uvw] (arrows in Fig. 4*D*) and likely associated with screw dislocations (Fig. 4 *D*, *iv*, dashed orange lines). Based on FFT patterns (*SI Appendix*, Fig. S18) of regions 1 to 7 in Fig. 4*D*, systematic changes in crystal orientation show an increasing shift in $\emptyset$ from 59 to 76° (Fig. 4*E* and *SI Appendix*, Figs. S18 and S19). The presence of screw dislocation is further confirmed by observation of helical distortions (atomic positions with helical ordering) in HRTEM images (*SI Appendix*, Fig. S20).

HRTEM images of bent segments (Fig. 4*F*) show a high density of edge dislocations (Fig. 4*G*). These defects are not aligned along a given singular orientation (Fig. 4*F*); however, most of the dislocations are distributed in the [10$\bar{2}$] direction with a minority oriented in a nearly orthogonal [31$\bar{3}$] direction. The latter seemingly occur in severely strained areas, as shown in Fig. 4*F*. A discontinuous layer forms the half-atomic plane for an edge dislocation along the [31$\bar{3}$] direction. The Burgers vectors are along different slip systems (63, 64), resulting in distributed defects in the convex side of bent crystals. The distortion is responsible for the moiré fringes with d-spacing similar to $2x\vec{b}$ or 0.68 nm (*SI Appendix*, Fig. S17*B*). The distortion in the lattice is directly associated to screw dislocations in the <111> directions, which change the d-spacings from the convex (1.36 nm) to concave (1.52 nm) sides (*SI Appendix*, Fig. S17). In addition, Moiré distortion is evident within bent segments (*SI Appendix*, Fig. S17 *B–D*), suggesting a twist between adjacent layers induced by screw dislocations (65, 66). SEM images of NH_4HU rod-like crystals reveal twisting at both ends (*SI Appendix*, Fig. S2). According to the mechanism proposed by Eshelby (54), screw dislocations produce inner strain that relaxes stress within twisted crystals (Fig. 1*F*). This is consistent with HRTEM images showing a higher percentage of edge dislocations on the convex side of bent segments (Fig. 4*D*) with screw dislocations located in distorted regions (e.g., Fig. 4 *D*, *iv*, dashed orange lines). Collectively, the synergistic effect between screw and edge dislocations drives spontaneous (bottom–up) bending and twisting during crystallization. These dislocations are likely formed through a disruption of aromatic stacking, which we hypothesize is a result of defects created by the interactions with or occlusion of minor tautomer molecules.

Models in the literature describing crystal bending under an applied strain (13, 67–69) are typically associated with plastic deformation. Acicular crystals are usually bent by applying force at the two opposite termini of the crystal, or by the three-point method where the crystal is supported perpendicular to its length at both ends from one side and pressed at the middle section from the opposite side. These compressive and tensile stresses are often

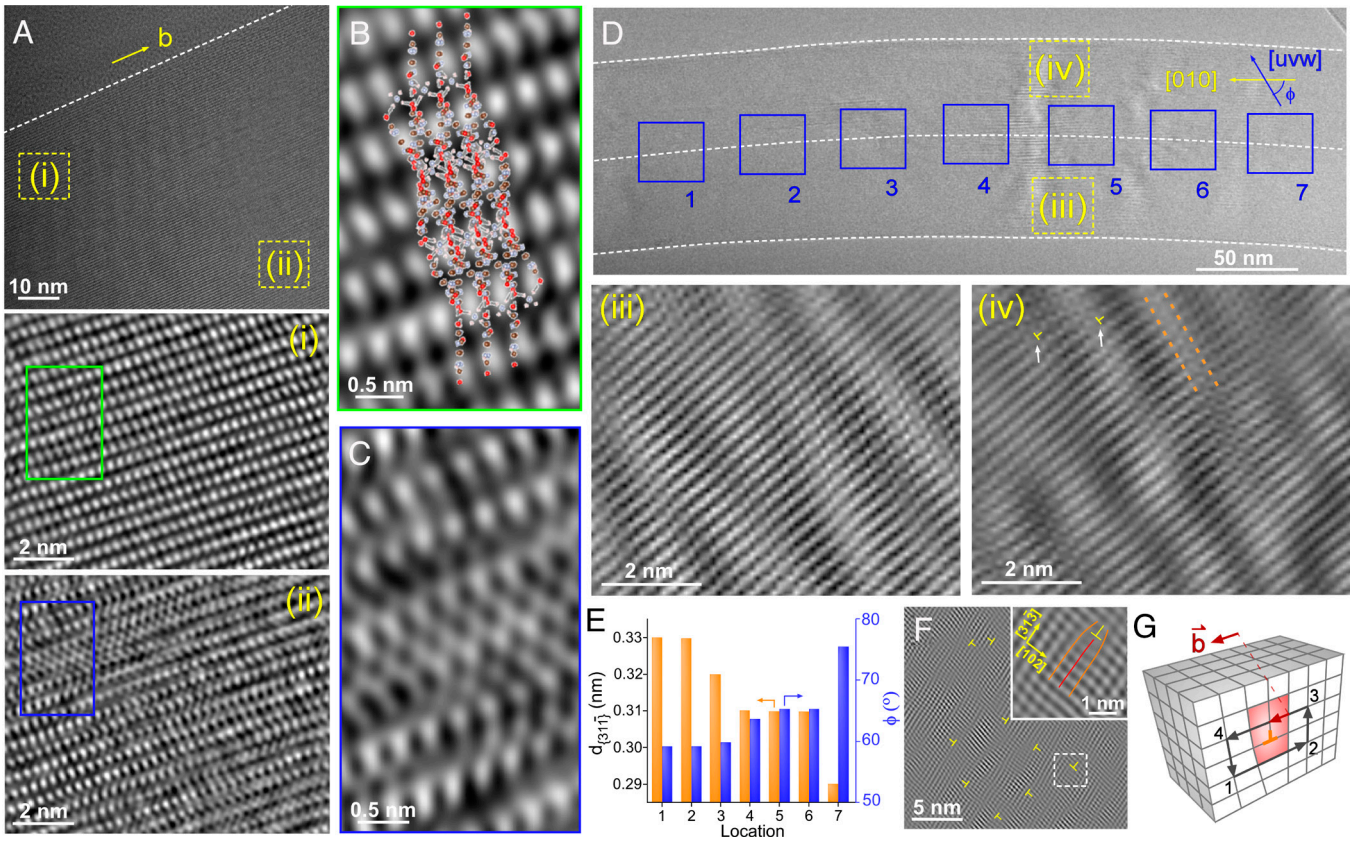

Fig. 4. Collection and analysis of high-resolution TEM images for bent NH_4HU crystals prepared at pH 7. (*A*) HRTEM image of the straight segment of a bent crystal showing the atomic clusters of the structure with enlarged filtered images of dashed boxes showing the absence (i) and presence (ii) of random defects. (*B*) Enlarged filtered image of the green dashed box in panel (i) showing the well-organized lattice strips overlaid with the crystal structure model of the NH_4HU [100] zone axis. (*C*) Enlarged filtered image of the blue dashed box in panel (ii) showing random stacking faults. (*D*) HRTEM image of a bent segment after overlapping 10 low-dose images with a low fractionation technique in the TEAM 1 electron microscope with a Cc Corrector and a K2 Camera (see Methods). Images (iii) and (iv) are magnified areas showing molecular packing arrangements with the prevalence of dislocations toward the convex side of crystals. The parallel dashed lines indicate a screw dislocation with Burgers vector $\vec{b}_{[111]} = 0.34$ nm and yellow ⊥ symbols (with arrows) highlight edge dislocations. (*E*) Interplanar $d_{(hkl)}$ spacing of the $(31\bar{1})$ plane and angle ϕ = [uvw] ∩ [010] at locations 1 to 7 along the longitudinal direction of a bent crystal in panel *D*. (*F*) IFFT TEM image showing the presence of multiple edge dislocations (⊥ symbols). The image is produced by combining ten low-dose experimental images and Fourier filtering to show atomic clusters of the bent crystal. Insert: enlarged filtered image of the white box highlighting an edge dislocation. (*G*) Schematic representation of an edge dislocation with the Burgers vector (red arrow).

regularly accompanied by sliding of molecular layers (13), whereby the individual layers glide but remain in contact with each other to preserve the macroscopic integrity of the bent crystal (67); however, natural bending and twisting of tautomeric NH_4HU crystals can be attributed to an alternative mechanism based on the synergistic effect between screw and edge dislocations. These defects are not the byproduct of an applied strain, but rather occur in situ during crystallization as a result of growth modifiers (minor tautomer) that we believe are responsible for generating defects along the fastest growth direction. The accumulation of defects on convex sides of bent crystals may be associated with an imbalanced torque induced by axial screw dislocations with opposite handedness located at the ends of rod-like crystals (*vide infra*). The exact mechanism for defect formation by the minor tautomer is not fully understood, but it is evident these features differ from examples in literature where deformations generated under applied strain involve flexible layers sliding on top of each other to enable crystal bending.

The observed shifts in lattice parameters are attributed to the distorted intermolecular interactions from bending and twisting that impose internal strain on NH_4HU crystals. These effects were probed by two techniques. The first is photoinduced force microscopy (PiFM), which combines infrared (IR) and AFM to spatially resolve differences in both chemistry and local structure at sub-5-nm resolution (*SI Appendix*, Fig. S21) (70). Cross-sectional analysis of a straight crystal reveals no appreciable change in IR spectra (Fig. 5 *A*–*C* and *SI Appendix*, Fig. S22); however, the same analysis of a bent crystal (Fig. 5 *D*–*F*) reveals a gradual change in IR spectra (Fig. 5*G*) from the concave (*cc*, scan 1) to convex (*cx*, scan 15) locations. A broadening and intensity reduction of the IR peak at ~1,397 cm^{-1} (Fig. 5*G*, red shading) corresponds to the modification of the N-H wagging mode, δ_r(N-H), which may be associated with the generation of twins and edge dislocations on the convex side of the bent crystal. Moreover, the intensity of the ν_s(C-N) mode at ~1,009 cm^{-1} (Fig. 5*G*, purple shading), which is associated with π–π interactions, decreases from the concave to convex side, consistent with the increasing $d_{(hkl)}$ spacing of (002) and (202) planes. We also observe shifts at 1,673 cm^{-1} (Fig. 5*G*, gray shading) corresponding to the asymmetrical vibration mode of C=O. A blueshift of this band indicates weaker urate–ammonium interactions on the convex side of the bent crystal. Comparison of PiFM data of cross-sections at the point of maximum bending to solid-state IR measurements obtained on bulk powders of the same bent NH_4HU crystal sample (Fig. 5*G*, green spectrum) highlights differences between surface and bulk properties, respectively. This is a general phenomenon that is also observed in the analysis of straight crystals (*SI Appendix*, Figs. S22 and S23). Chemically selective PiFM imaging performed over larger regions of straight and bent NH_4HU crystals reveal that the cross-sectional analysis is consistent over much broader regions.

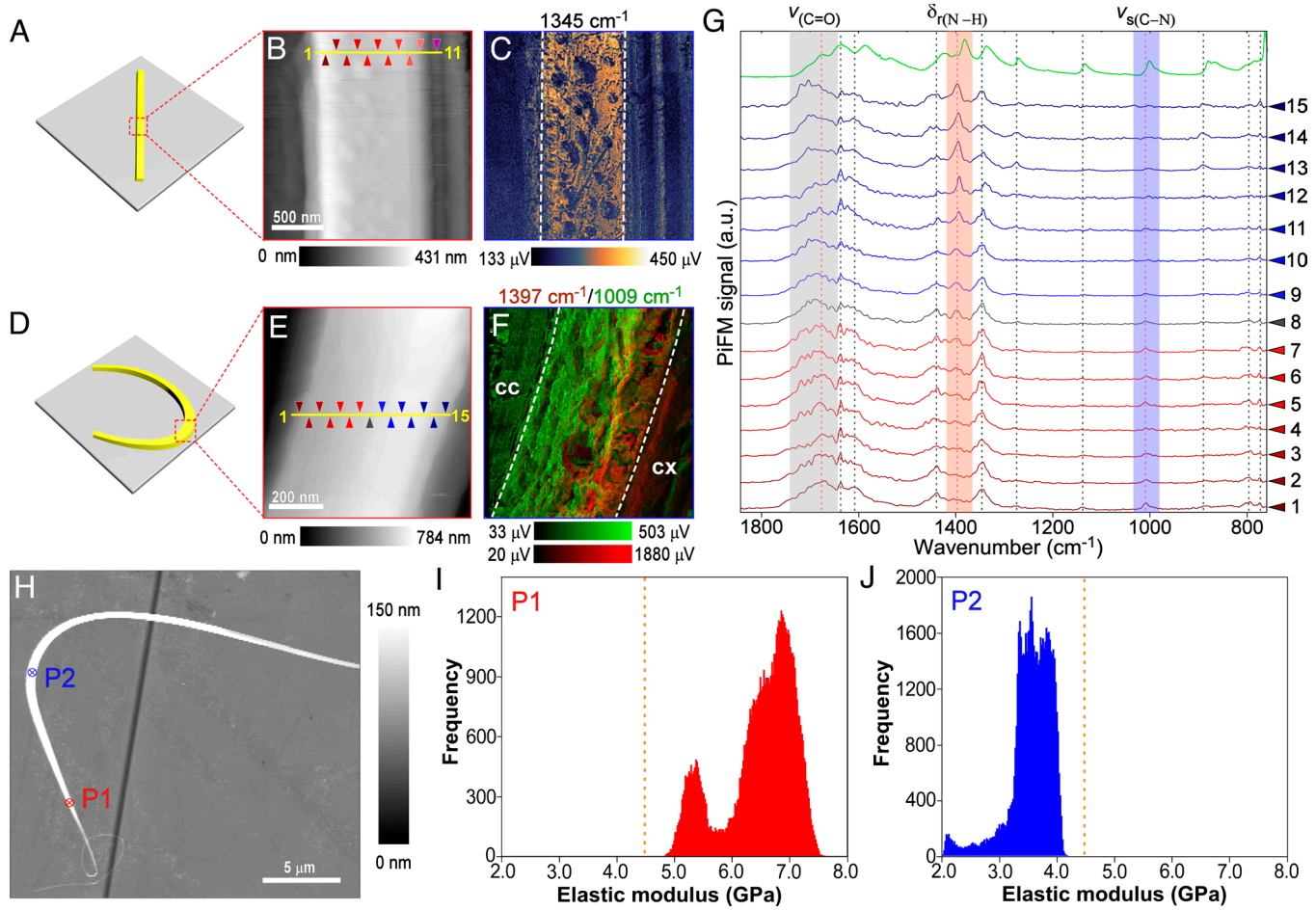

Fig. 5. Spatially resolved changes in intermolecular interactions and nanomechanical properties. (*A*–*G*) PiFM imaging of straight and bent NH_4HU crystals with (*A* and *D*) schematic representations, (*B* and *E*) AFM topography images, and (*C* and *F*) chemical mapping images at 1,345 cm^{-1} (*C*) and superimposing 1,397 cm^{-1} (red) and 1,009 cm^{-1} (green) peaks in the IR spectra (*F*). The yellow line in (*B*) with points 1 to 11 traverses a cross-sectional region used for collecting PiF-IR spectra (*SI Appendix*, Fig. S21). The yellow line in (*E*) with points 1 to 15 traverses a cross-sectional region used for collecting (*G*) spatially resolved PiF-IR spectra compared to the analysis of the bulk sample (green spectrum). Chemical imaging of a straight crystal shows a homogenous feature on the basal surface at 1,345 cm^{-1} (panel *C*) and other IR wavelengths (*SI Appendix*, Fig. S24); however, the bent crystal displays much more heterogeneous patterns. For instance, the intensity of PiFM imaging at 1,397 cm^{-1} is significantly stronger on the convex side of the bent crystal (*SI Appendix*, Fig. S25). This is also true for other IR bands such as 1,704, 1,690, 1,345, and 1,275 cm^{-1}. On the contrary, the PiFM image intensity at 1,009 cm^{-1} is stronger on the concave side. A similar trend is observed at 1,138 cm^{-1}. The heterogeneity is clearly observed in (*F*) when overlaying the chemical PiFM imaging at 1,397 cm^{-1} with 1,009 cm^{-1}. (*H*–*J*) Contact resonance AFM analysis of the elastic modulus for the (*I*) straight segment (P1, red) and (*J*) bent segment (P2, blue) of the NH_4HU crystal shown in panel (*H*).

The second technique used to probe strain in NH_4HU crystals is contact resonance AFM, which can be used to extract spatial variation in the elastic modulus (71, 72). Analysis was performed in two locations corresponding to the ends (P1) where the crystal is relatively straight without significant twisting, and a second region toward the center (P2) where there is a high degree of bending (Fig. 5*H*). Estimation of the elastic modulus of the two regions reveals higher values in the straight region (Fig. 5*I*) compared to the bent region (Fig. 5*J*), signifying the presence of defects reduces elasticity by nearly a factor of two. This is consistent with our previous study (36) showing that bent regions are softer and more prone to dissolve at faster rates when exposed to an undersaturated solution.

Conclusions

In summary, we provide an example of naturally bent and twisted crystals that were created without using conditions typically required to achieve these features, which include (but are not limited to) an applied strain, photonic/thermal induction, the incorporation of foreign impurities, or the generation of cocrystals. We attribute the unique behavior of NH_4HU to the keto–enol tautomerism of the biogenic urate molecule. It is evident that bending/twisting is more prevalent under growth conditions where there is a higher concentration of minor tautomer, which functions as a native growth modifier of NH_4HU crystallization. These crystals display a high density of dislocations which increases with urate concentration. Left-and right-handed twisted crystals are nearly equal in number, without evidence of spontaneous symmetry breaking. Although the exact mechanism remains elusive, defects in the form of edge and screw dislocations, twins, and stacking faults are created in situ during crystal growth; and the extent of bending and branching can be tuned by adjusting the supersaturation. We use a combination of state-of-the-art microscopy and spectroscopy techniques to probe different locations of NH_4HU crystals along axial and cross-sections of straight and bent segments. TEM analysis confirmed systematic shifts in d-spacings wherein dislocations are predominantly oriented along a single direction, which leads to a gradual change in orientation with bending. This mechanism is in stark contrast to plastic deformation models proposed in literature to explain bending under an applied strain. Here, the synergistic process of bending and twisting occurs as a result of defects accumulated during crystal growth. When evaluating cross-sections of bent crystals, we

observe a disproportionately higher number of defects on the convex side. This is consistent with PiFM analysis showing systematic changes in the intermolecular interactions, which, in turn, generate internal strain. This was quantitatively assessed by contact resonance AFM measurements of NH_4HU crystals to confirm differences in the mechanical properties of straight and bent segments. We postulate that bending deformation may be associated with an imbalanced torque induced by twist deformations at each end of rod-like crystals in accordance with the Eshelby twist mechanism; therefore, the synergistic effect of screw and edge dislocations likely induces spontaneous bending and twisting of NH_4HU crystals.

Our findings provide a greater understanding of the defects generated during pathological crystallization of a tautomeric material (e.g., cetacean NH_4HU kidney stones) and how this phenomenon can lead to unique bent, twisted, and dendritic morphologies observed in both biological and synthetic materials. The ability to selectively control this behavior opens broad avenues for crystal engineering. For example, tailoring the mechanical properties of crystals can impact their kinetics of dissolution (36), which has practical implications for the design of new therapeutics to treat NH_4HU kidney stones. Given the widespread examples of tautomeric crystals in nature and commercial applications (e.g., pharmaceuticals, optical and electrical devices, etc.), we believe the results of this study may have relevance for understanding and controlling the impact of minor tautomer(s) on crystallization of a broader range of materials.

Materials and Methods

All Materials and Methods are reported in detail within *SI Appendix* and are briefly summarized below.

Bulk Crystallization Assays. Ammonium urate (NH_4HU) crystals were synthesized by dissolving appropriate amounts of anhydrous uric acid (UA) powder in 100 mL glass bottles containing deionized (DI) water and adjusting the solution to pH 6 with 28 wt% ammonium hydroxide ($NH_3{\cdot}H_2O$) under rapid agitation at 72 °C. The resultant solution (pH 7) was left at 21 ± 1 °C for at least 24 h to allow crystallization. The prepared solutions vary in their concentrations from 5 to 10 mM. The solution pH was measured using an Orion Dual Star pH benchtop meter with a ROSS Ultra electrode (8102BNUWP). The crystalline product (in solution) was observed by optical microscopy using a Leica DMi8 instrument. Crystals were also extracted at periodic times and dried in air overnight. The crystalline phase of crystals was analyzed with a Siemens D5000 X-ray diffractometer (XRD) using a Cu Kα source (40 kV, 30 mA) and was confirmed by a reference pattern from the solved crystal structure (*vide infra*). Ex situ microscopy measurements were performed using an FEI 235 dual-beam focused ion beam scanning electron microscopy (SEM). The samples for SEM were coated with ca. 20 nm gold to reduce the effects of electron beam charging.

Preparation of NH_4HU Crystal Seeds. Ammonium urate crystal seeds were prepared by two steps: the spontaneous crystallization from a concentration of 7.5 mM NH_4HU at pH 11; and the transfer of this suspension into 400 mL freshly prepared 5.5 mM NH_4HU growth solution (pH 11) in a 500 mL glass bottle. The NH_4HU solution was prepared by dissolving appropriate amounts of UA anhydrous powder in DI water and adjusting the solution to pH 10.2 with 28 wt% ammonium hydroxide ($NH_3{\cdot}H_2O$) under rapid agitation at 72 °C. The resultant solution (pH 11) was left at 21 ± 1 °C for 48 h to allow crystallization, and the obtained crystals were transferred into a 5.5 mM NH_4HU growth solution for a 7-d incubation period to produce needle-like crystals of length 10 to 50 μm and width <1 μm. To increase the width of NH_4HU crystals, the product after 7 d of growth was recovered by filtration, and the solids were placed into another 5.5 mM NH_4HU growth solution for further incubation. The two-step seeded growth procedure produces crystals with a width of 1 to 2 μm.

Electron Microscopy. Crystals were directly deposited onto the copper grid with lacey carbon film without crushing in order to keep their original morphology. The TEM experiments were conducted on a Thermal Fisher Themis-Z microscope. A double tilt holder was used for NED experiments and a Fischione model 2020 tomography holder was used for three-dimensional electron diffraction (3DED) and tomography experiments. A Gatan Oneview detector was used for collecting all datasets.

3DED and NED. The microscope was operated in STEM mode. A quasi-parallel probe was obtained by adjusting the current of the C3 lens so that a sharp central spot could be observed on the fluorescence screen. A 10 μm C2 aperture was used to obtain a quasi-parallel probe with a size of approximately 40 nm in diameter. The beam position can be controlled using Velox or TIA software for collecting NED patterns from a local region. The camera length was kept at 230 cm. During 3DED data collection, the position of the target crystal was tracked using the HAADF image stream during stage rotation. The tilt range for each dataset was close to 120°. The exposure time was 1 s, and the rotation speed was around 0.6°/s. The electron dose rate was adjusted to 0.2 e $Å^{-2}$ s^{-1}, and the total electron dose was approximately 40 e $Å^{-2}$ for each dataset.

TEM tomography. During tomography data collection, the microscope was operated in TEM imaging mode. The magnification was adjusted to 17,000. The exposure time was 2 s. A tilt series of bright-field TEM images of the target sample was acquired over an angular range from −70 to +70°. The interval between neighboring images was kept at 1.0°. Before the sample was placed on the copper grid, a droplet of a 5 nm gold nanoparticle dispersion was also delivered onto the copper grid as a fiducial marker for tomogram alignment. The software ETomo was used for tilt series data processing, which included alignment and reconstruction.

Analysis of crystal defects. High-resolution TEM observations were performed on the TEAM I electron microscope (NCEM-Molecular Foundry Lawrence Berkeley National Laboratory) by dose fractionation with low dose rates. In brief, the microscope is operated using a Nelsonian illumination (73), a Cc corrector (74), and a K2 camera (75). The illumination creates a pencil-like, highly coherent beam of $\triangle E \lesssim 100$ meV that matches the field of view (FoV) of the K2 camera (~10^7 $Å^2$ at high resolution with apparent pixel size of 0.3 * 0.3 $Å^2$). This approach allows for the detection of single electron scattering events with dose rates that suppress the degradation of structure information with dose accumulation that is common to radiation-sensitive matter. It also maintains high standards for aberration corrections (76).

Data, Materials, and Software Availability. All study data are included in the article and/or supporting information.

ACKNOWLEDGMENTS. JDR acknowledges financial support from the Office of Navy Research (Grant Nos. N00014-21-1-2173 and N00014-20-1-2083), The Welch Foundation (Grant No. E-1794), and the Welch Foundation Center for Advanced Bioactive Materials Crystallization (Grant No. V-E-0001). WT acknowledges financial support from the National Natural Science Foundation of China (Grant No. NNSFC 22278300). XZ received financial support from the Swedish research council (Grant Nos. VR 2017-04321 and VR 2019-00815) and the Knut & Alice Wallenberg Foundation (Grant Nos. 2012.0112 and 2018.0237). Electron microscopy is supported by the Molecular Foundry, which is supported by the Office of Science, the Office of Basic Energy Sciences, the US Department of Energy under Grant No. DE-AC02-05CH11231 (proposal 6225). Q.T. acknowledges support from the NSF (Grant No. CMMI-2311573).

Author affiliations: [a]Department of Chemical and Biomolecular Engineering, University of Houston, Houston, TX 77204; [b]School of Chemical Engineering and Technology, State Key Laboratory of Chemical Engineering and Low-Carbon Technology, The Co-Innovation Center of Chemistry and Chemical Engineering of Tianjin, Tianjin University, Tianjin 300072, China; [c]Department of Materials and Environmental Chemistry, Stockholm University, Stockholm SE-106 91, Sweden; [d]Department of Materials Science and Engineering, Texas A&M University, College Station, TX 77843; [e]Instituto Politecnico Nacional (IPN), Escuela Superior de Física y Matemáticas-IPN, Departamento de Física, Unidad Profesional Adolfo López Mateos Zacatenco, Ciudad de México 07338, Mexico; [f]The Molecular Foundry, Lawrence Berkeley National Laboratory, Berkeley, CA 94720; [g]Cullen College of Engineering, Division of Technology, Engineering Technology, Houston, TX 77009; and [h]Molecular Vista Inc., San Jose, CA 95119

1. J. A. Rogers, T. Someya, Y. Huang, Materials and mechanics for stretchable electronics. *Science* **327**, 1603–1607 (2010).
2. X. Yang *et al.*, Electrically conductive hybrid organic crystals as flexible optical waveguides. *Nat. Commun.* **13**, 7874 (2022).
3. D. P. Karothu *et al.*, Global analysis of the mechanical properties of organic crystals. *Angew. Chem. Int. Ed.* **61**, e202113988 (2022).
4. S. K. Park *et al.*, Super- and ferroelastic organic semiconductors for ultraflexible single-crystal electronics. *Angew. Chem. Int. Ed.* **59**, 13004–13012 (2020).
5. M. Annadhasan *et al.*, Micromanipulation of mechanically compliant organic single-crystal optical microwaveguides. *Angew. Chem. Int. Ed.* **59**, 13821–13830 (2020).
6. M. Annadhasan *et al.*, Mechanophotonics: Flexible single-crystal organic waveguides and circuits. *Angew. Chem. Int. Ed.* **59**, 13852–13858 (2020).
7. M. Annadhasan, S. Basak, N. Chandrasekhar, R. Chandrasekar, Next-generation organic photonics: The emergence of flexible crystal optical waveguides. *Adv. Opt. Mater.* **8**, 2000959 (2020).
8. F. Ilievski, A. D. Mazzeo, R. F. Shepherd, X. Chen, G. M. Whitesides, Soft robotics for chemists. *Angew. Chem. Int. Ed.* **50**, 1890–1895 (2011).
9. E. Ahmed, D. P. Karothu, M. Warren, P. Naumov, Shape-memory effects in molecular crystals. *Nat. Commun.* **10**, 3723 (2019).
10. J. Mahmoud Halabi, E. Ahmed, S. Sofela, P. Naumov, Performance of molecular crystals in conversion of light to mechanical work. *Proc. Natl. Acad. Sci. U.S.A.* **118**, e2020604118 (2021).
11. W. Talataisong, R. Ismaeel, G. Brambilla, A review of microfiber-based temperature sensors. *Sensors* **18**, 461 (2018).
12. A. G. Shtukenberg, Y. O. Punin, A. Gujral, B. Kahr, Growth actuated bending and twisting of single crystals. *Angew. Chem. Int. Ed.* **53**, 672–699 (2014).
13. P. Commins, D. P. Karothu, P. Naumov, Is a bent crystal still a single crystal?. *Angew. Chem. Int. Ed.* **58**, 10052–10060 (2019).
14. M. Zorz, Quarz-gwindel. *Mineralien der Welt* **20**, 30–46 (2009).
15. H. A. Miers, *Mineralogy: An Introduction to the Scientific Study of Minerals* (Macmillan and Company, limited, 1902).
16. M. Maleev, *Properties and Genesis of Natural Thread-like Crystals and Aggregates* (Nauka, Moskau, 1971).
17. W. Du *et al.*, Twisting, untwisting, and retwisting of elastic Co-based nanohelices. *Nat. Commun.* **14**, 4426 (2023).
18. Y. Chen, Z. Chang, J. Zhang, J. Gong, Bending for better: Flexible organic single crystals with controllable curvature and curvature-related conductivity for customized electronic devices. *Angew. Chem. Int. Ed.* **60**, 22424–22431 (2021).
19. A. G. Shtukenberg, X. Zhu, Y. Yang, B. Kahr, Common occurrence of twisted molecular crystal morphologies from the melt. *Cryst. Growth Des.* **20**, 6186–6197 (2020).
20. B. Kahr *et al.*, Crystals of benzamide, the first polymorphous molecular compound, are helicoidal. *Angew. Chem. Int. Ed.* **59**, 14593–14601 (2020).
21. D. W. Davies *et al.*, Unraveling two distinct polymorph transition mechanisms in one n-type single crystal for dynamic electronics. *Nat. Commun.* **14**, 1304 (2023).
22. K. Yadava, X. Qin, X. Liu, J. J. Vittal, Straight, bendable and bent organic crystals. *Chem. Commun.* **55**, 14749–14752 (2019).
23. Y. Chen, B. Jing, Z. Chang, J. Gong, Luminescent möbius strip of a flexible halogen-bonded cocrystal evolved from ring and helix. *JACS Au* **2**, 2686–2692 (2022).
24. D. Kitagawa, H. Nishi, S. Kobatake, Photoinduced twisting of a photochromic diarylethene crystal. *Angew. Chem. Int. Ed.* **52**, 9320–9322 (2013).
25. L. Zhu, R. O. Al-Kaysi, C. J. Bardeen, Reversible photoinduced twisting of molecular crystal microribbons. *J. Am. Chem. Soc.* **133**, 12569–12575 (2011).
26. D. Kitagawa, S. Kobatake, Photoreversible current on/off switching by the photoinduced bending of gold-coated diarylethene crystals. *Chem. Commun.* **51**, 4421–4424 (2015).
27. R. Rai, B. P. Krishnan, K. M. Sureshan, Chirality-controlled spontaneous twisting of crystals due to thermal topochemical reaction. *Proc. Natl. Acad. Sci. U.S.A.* **115**, 2896–2901 (2018).
28. S. Saha, M. K. Mishra, C. M. Reddy, G. R. Desiraju, From molecules to interactions to crystal engineering: Mechanical properties of organic solids. *Acc. Chem. Res.* **51**, 2957–2967 (2018).
29. L. O. Alimi, P. Lama, V. J. Smith, L. J. Barbour, Hand-twistable plastically deformable crystals of a rigid small organic molecule. *Chem. Commun.* **54**, 2994–2997 (2018).
30. S. Saha, G. R. Desiraju, Crystal engineering of hand-twisted helical crystals. *J. Am. Chem. Soc.* **139**, 1975–1983 (2017).
31. L. Pejov, M. K. Panda, T. Moriwaki, P. Naumov, Probing structural perturbation in a bent molecular crystal with synchrotron infrared microspectroscopy and periodic density functional theory calculations. *J. Am. Chem. Soc.* **139**, 2318–2328 (2017).
32. G. R. Krishna, R. Devarapalli, G. Lal, C. M. Reddy, Mechanically flexible organic crystals achieved by introducing weak interactions in structure: Supramolecular shape synthons. *J. Am. Chem. Soc.* **138**, 13561–13567 (2016).
33. C. M. Reddy *et al.*, Structural basis for bending of organic crystals. *Chem. Commun.* **21**, 3945–3947 (2005).
34. S. Ghosh, M. K. Mishra, S. Ganguly, G. R. Desiraju, Dual stress and thermally driven mechanical properties of the same organic crystal: 2, 6-dichlorobenzylidene-4-fluoro-3-nitroaniline. *J. Am. Chem. Soc.* **137**, 9912–9921 (2015).
35. M. Rohullah, V. V. Pradeep, J. Ravi, A. V. Kumar, R. Chandrasekar, Micromechanically-powered rolling locomotion of a twisted-crystal optical-waveguide cavity as a mobile light polarization rotor. *Angew. Chem. Int. Ed.* **61**, e202202114 (2022).
36. W. Tang *et al.*, Tautomerism unveils a self-inhibition mechanism of crystallization. *Nat. Commun.* **14**, 561 (2023).
37. N. Pinsk *et al.*, Biogenic guanine crystals are solid solutions of guanine and other purine metabolites. *J. Am. Chem. Soc.* **144**, 5180–5189 (2022).
38. D. Gur *et al.*, Guanine crystallization in aqueous solutions enables control over crystal size and polymorphism. *Cryst. Growth Des.* **16**, 4975–4980 (2016).
39. B. Hernández, F. J. Luque, M. Orozco, Tautomerism of xanthine oxidase substrates hypoxanthine and allopurinol. *J. Org. Chem.* **61**, 5964–5971 (1996).
40. P. Pospisil, P. Ballmer, L. Scapozza, G. Folkers, Tautomerism in computer-aided drug design. *J. Recept. Signal Transduct. Res.* **23**, 361–371 (2003).
41. L. Antonov, *Tautomerism: Methods and Theories* (John Wiley & Sons, 2013).
42. D. Wang *et al.*, Ketone–enol tautomerism, polymorphism, mechanofluorochromism and solid-state acidochromism of isoquinolinone–arylidenehydrazine derivatives. *J. Mater. Chem. C* **9**, 12868–12876 (2021).
43. S.-Q. Wu *et al.*, Macroscopic polarization change via electron transfer in a valence tautomeric cobalt complex. *Nat. Commun.* **11**, 1992 (2020).
44. O. Sato, A. Cui, R. Matsuda, J. Tao, S. Hayami, Photo-induced valence tautomerism in Co complexes. *Acc. Chem. Res.* **40**, 361–369 (2007).
45. L. Antonov *et al.*, Exploiting tautomerism for switching and signaling. *Angew. Chem. Int. Ed.* **48**, 7875–7878 (2009).
46. P. Naumov *et al.*, The rise of the dynamic crystals. *J. Am. Chem. Soc.* **142**, 13256–13272 (2020).
47. L. Guasch *et al.*, Experimental and chemoinformatics study of tautomerism in a database of commercially available screening samples. *J. Chem. Inf. Model.* **56**, 2149–2161 (2016).
48. X. Geng, J. Meegan, C. Smith, K. Sakhaee, J. D. Rimer, Crystallization of hierarchical ammonium urate: Insight into the formation of cetacean renal stones. *Cryst. Growth Des.* **19**, 6727–6735 (2019).
49. K. Chaudhary, K. Malhotra, J. R. Sowers, A. Aroor, Uric acid – Key ingredient in the recipe for cardiorenal metabolic syndrome. *Cardiorenal Med.* **3**, 208–220 (2013).
50. R. E. Sours, D. A. Fink, J. A. Swift, Dyeing uric acid crystals with methylene blue. *J. Am. Chem. Soc.* **124**, 8630–8636 (2002).
51. F. Liu *et al.*, Molecular crystal mechanical properties altered via dopant inclusion. *Chem. Mater.* **32**, 3952–3959 (2020).
52. M. J. Bierman, Y. K. A. Lau, A. V. Kvit, A. L. Schmitt, S. Jin, Dislocation-driven nanowire growth and eshelby twist. *Science* **320**, 1060–1063 (2008).
53. Y. Liu *et al.*, Helical van der Waals crystals with discretized Eshelby twist. *Nature* **570**, 358–362 (2019).
54. J. D. Eshelby, Screw dislocations in thin rods. *J. Appl. Phys.* **24**, 176–179 (1953).
55. S. Mardix, A. R. Lang, G. Kowalski, A. P. W. Makepeace, On structure and twist in ZnS crystal whiskers. *Philos. Mag. A* **56**, 251–261 (1987).
56. J. F. J. Dippy, The rhythmic crystallization of melts. *J. Phys. Chem.* **36**, 2354–2361 (1932).
57. J. F. Nye, Some geometrical relations in dislocated crystals. *Acta Metall.* **1**, 153–162 (1953).
58. I. A. Olson, A. G. Shtukenberg, B. Kahr, M. D. Ward, Dislocations in molecular crystals. *Rep. Prog. Phys.* **81** (2018).
59. J. W. Mullin, Ed., *Crystallization* (Butterworth-Heinemann, Oxford, ed. 4, 2001).
60. W. K. Burton, N. Cabrera, F. C. Frank, Role of dislocations in crystal growth. *Nature* **163**, 398–399 (1949).
61. P. M. Anderson, J. P. Hirth, J. Lothe, *Theory of Dislocations* (Cambridge University Press, 2017).
62. D. Kuhlmann-Wilsdorf, The theory of dislocation-based crystal plasticity. *Philos. Mag. A* **79**, 955–1008 (1999).
63. Z. Gao *et al.*, High-throughput screening of 2D van der Waals crystals with plastic deformability. *Nat. Commun.* **13**, 7491 (2022).
64. T.-R. Wei *et al.*, Exceptional plasticity in the bulk single-crystalline van der Waals semiconductor InSe. *Science* **369**, 542–545 (2020).
65. K. F. Mak, J. Shan, Semiconductor moiré materials. *Nat. Nanotechnol.* **17**, 686–695 (2022).
66. Y. Cao *et al.*, Correlated insulator behaviour at half-filling in magic-angle graphene superlattices. *Nature* **556**, 80–84 (2018).
67. M. K. Panda *et al.*, Spatially resolved analysis of short-range structure perturbations in a plastically bent molecular crystal. *Nat. Chem.* **7**, 65–72 (2015).
68. P. Naumov, S. Chizhik, M. K. Panda, N. K. Nath, E. Boldyreva, Mechanically responsive molecular crystals. *Chem. Rev.* **115**, 12440–12490 (2015).
69. W. M. Awad *et al.*, Mechanical properties and peculiarities of molecular crystals. *Chem. Soc. Rev.* **52**, 3098–3169 (2023).
70. D. Nowak *et al.*, Nanoscale chemical imaging by photoinduced force microscopy. *Sci. Adv.* **2**, e1501571 (2016).
71. Q. Tu *et al.*, Quantitative subsurface atomic structure fingerprint for 2D materials and heterostructures by first-principles-calibrated contact-resonance atomic force microscopy. *ACS Nano* **10**, 6491–6500 (2016).
72. S. Zauscher, Z. Parlak, Q. Tu, "Mapping the stiffness of nanomaterials and thin films by acoustic AFM techniques" in *Handbook of Nanomaterials Properties*, B. Bhushan, D. Luo, S. R. Schricker, W. Sigmund, S. Zauscher, Eds. (Springer, Berlin Heidelberg, Berlin, Heidelberg, 2014), pp. 1023–1051.
73. C. Kisielowski, On the pressing need to address beam–sample interactions in atomic resolution electron microscopy. *J. Mater. Sci.* **51**, 635–639 (2016).
74. R. Henderson, From electron crystallography to single particle cryoEM (Nobel lecture). *Angew. Chem. Int. Ed.* **57**, 10804–10825 (2018).
75. P. Grob *et al.*, Ranking TEM cameras by their response to electron shot noise. *Ultramicroscopy* **133**, 1–7 (2013).
76. C. Kisielowski *et al.*, Instrumental requirements for the detection of electron beam-induced object excitations at the single atom level in high-resolution transmission electron microscopy. *Micron* **68**, 186–193 (2015).